Surface Turbulence Measurements at Ohmsett

For:

**U.S. Department of the Interior
Minerals Management Service
Herndon, VA**

By

**Fabrice Veron,
Newark, Delaware**

**SL Ross Environmental Research Ltd.,
Ottawa, ON**

&

**MAR Inc.
Leonardo, New Jersey**

April 2009

SL ROSS

Acknowledgements

Disclaimer

Table of Contents

List of Figures

List of Tables

Introduction

The objective of this project was to measure the surface turbulence in the National Oil Spill Response Test Facility (Ohmsett) test tank located in Leonardo New Jersey under various wave configurations and compare these energies to those encountered in the field at specific sea-states. The tests were completed at Ohmsett the week of August 17th, 2008.

Background

When oil is spilled on the surface of the ocean, a thin film, which stretches under the action of gravity and surface tension forces, is formed and remains on the surface. However, under the influence of surface turbulence the film can disintegrate into small oil droplets, some of which can then be entrained to depth leading to an oil-in-water dispersion. The dispersion process can be influenced by the thickness of the film, surface tension, the level of turbulence and the presence of chemical treating agents (dispersants). This process can lead to the eventual dispersion and removal of the pollutant from the water surface. The turbulence at the surface responsible for the film break up is usually generated by breaking waves although other mechanisms such as rain impact can generate turbulence at the ocean surface. Turbulence generated by wind-induced shear near the surface[1] is generally weaker than the turbulence generated by breaking waves. Yet, breaking-wave generated turbulence is highly localized and occupies only a small fraction of the total ocean surface at a given time.

Theoretical investigation of droplet break-up and atomization were pioneered by Hinze (1955) who argued that the main controlling factor is the Weber number (We) which is the ratio of (destabilizing) shearing pressure forces to (stabilizing) surface tension forces. Hinze argued that there exists a critical value of the Weber number which predicts whether or not

---

[1] This would be analogous to the turbulence generated in wall bounded flow, adjacent to a solid flat surface.

a drop will be stable or broken up in a given turbulent flow. Then, based on the turbulent energy dissipation rate, he predicted a maximum stable drop size.

There have been a number of studies examining the break up of films and the generation of droplets and emulsions, with both mechanical stirrers and in some cases surface breaking waves (Rallison 1984; Delvigne and Sweeney, 1988; Stone, 1994). These generally conclude that the droplet size distribution is dependent on the surface tension and viscosity (and other chemical properties of the spilled product) and on the mechanical energy dissipated by the turbulence. These studies ordinarily attribute the breakup of large droplets (as opposed to the conversion of a thin film of oil to droplets) to the shear forces generated by the (small) turbulent eddies on the (large) droplet boundaries. Turbulent pressure forces and turbulence shear forces are the main mechanisms for the breakup of large oil droplets into smaller drops. Both mechanisms lead to comparable *maximum* drop sizes but the two mechanisms have different dependencies on surface tension that can lead to different droplet size *distributions*. This is significant since surface tension reduction through the use of surface-active chemical additives (chemical dispersants) will affect these processes. The ultimate size distribution of an oil dispersion is critical with regard to mitigation because small oil drops with radii on the order of tens of microns will likely be diffused within the water column and rapidly degrade, while large drops may return to the surface and contaminate wildlife and shores. Yet, an even more fundamental issue lies in the generation of the turbulence at the very interface where the oil film resides (as opposed to the breakup of droplets of oil to smaller drops); turbulence which in turn will lead to the initial atomization of the film. Despite our understanding of the mechanisms that generate surface turbulence which we can attribute in large part to the wind shear and breaking waves, very little is still known about the turbulence levels generated on the interface itself.

The generation of the turbulence at the air-sea interface is mostly due to breaking waves but making detailed measurement at the air-sea interface has proven extremely difficult in all but the most benign conditions. This has led to the development of novel measurement techniques to quantify processes at the air-sea interface. An infrared technique has been

developed to simultaneously study multiple aspects of the air-sea interface. The instrumentation comprised an active and passive optical and infrared imaging system accompanied with a motion package. An eddy covariance met package was also deployed along with an underwater Acoustic Doppler Current and Wave Profiler. The instruments have been tested and deployed during several field experiments in the Pacific off the coast of Southern California and in the near-shore from the Pier at Scripps Institution of Oceanography. Details can be found in Veron et al. 2008a, 2008b, 2009. The technique permits the detailed study of the ocean surface temperature and velocity fields. It has been shown that cross-correlation techniques typically used in particle image velocimetry can be used to infer the ocean surface velocity and kinematic fields from passive infrared temperature images.

In the work reported here, and in conjunction with single point turbulence measurements and ultrasonic altimetry, thermal imaging was used to image the surface temperature skin layer at Ohmsett, under various wave conditions, to directly measure the surface turbulence. The surface velocity fields obtained from the infrared imagery analysis were then used to directly infer the surface turbulent kinetic energy dissipation. Comparisons with estimates relevant to field situations are offered.

3

Objectives

Knowing how the turbulent energy of a laboratory or wave tank test relates to various sea-states is an essential piece of information when trying to relate the results of laboratory or tank tests to operational situations. The main attractions of bench scale testing are the ease and minimal cost of testing which allows a large number of test variables to be studied quickly and inexpensively. The downside is the lack of field-realism present in the small scale. Field tests, on the other extreme, offer realism but at great cost and difficulty. Testing at Ohmsett provides an intermediate scale of testing with considerably reduced costs compared to full-field testing but with much more realistic test conditions than bench-scale testing. It is still necessary to quantify the turbulent kinetic energies in the Ohmsett tank that are important in the chemical dispersion process so the test results can be directly related to likely field performance at a particular sea state. Being able to control the wave energy level at Ohmsett to match a specific sea state opens up a wider range of testing options for the Ohmsett facility. The objective of this project was to measure the surface turbulence at Ohmsett under various wave configurations and compare these energies to those encountered in the field at specific sea-states. There are three basic mixing energies of primary significance in the dispersion process. These include the process that mixes dispersant into the oil, the energy that breaks the treated oil into small droplets and the larger scale energy that mixes the droplets of oil down into the water column. This report focuses on the quantification of the surface turbulence available to break the treated slick into a fine-drop, oil-in-water dispersion. Because of the shallow depth of the Ohmsett tank the third mixing process cannot be fully simulated at Ohmsett. The mixing of applied dispersant into the oil versus water is an important short-term process but it is not the critical component except where viscous oils or emulsions are involved.

Experimental Setup

Wave tank

The experiments describe here were performed in the large water wave tank at the Ohmsett facility is located at the Naval Weapons Station Earle in Leonardo, New Jersey. The outdoors concrete tank is one of the largest of its kind, measuring 203 meters long by 20 meters wide by 3.5 meters deep (figure 1). The tank is filled with 10 million liters of water kept at ambient temperature. During this test series the water salinity was 28.5 ppt. This is slightly fresher than open ocean conditions. The tank is equipped with three movable bridges with adjustable tow speed and fixed position. For the experiments reported here, the instruments were all affixed to the main bridge that was subsequently positioned at three fixed locations (70m, 100m, and 130m from the wave maker; table 1).

Figure 1: Photograph of the wave tank at Ohmsett.

The tank is equipped with a wave maker capable of generating monochromatic waves at frequencies ranging from 0.2Hz to 0.75Hz. Depending on frequency, sinusoidal wave

amplitudes up to 0.7m can be generated (the wave maker uses strokes of 7.65cm, 15.3cm and 22.95cm). For the experiments presented here, the frequency range utilized varied from 0.33Hz to 0.66Hz and the significant wave height observed ranged from 0.27m to 0.57m (see table 1).

Instrumentation

Altimeter - A single point ultrasonic altimeter (Banner Engineering, model QT50ULB) was placed on the railing of the bridge, looking down at the water surface in order to measure the wave displacement (figure 2). The ultrasonic altimeter was sampled at a rate of 200Hz using a National Instrument sampling board (NI USB-6221). The altimeter response time is 100ms leading to a final effective temporal resolution of 10Hz. The range resolution of the altimeter is approximately 4mm (slightly temperature dependant). For each run, the surface displacement was recorded for 409.6 seconds (6min 49s 6/10s).

ADV Current Meter - The instruments used for the experiments comprised a single point acoustic Doppler velocimeter (ADV Sontek). The ADV was placed at a depth of 53.3cm from the still water surface in order to have its measurement volume remain submerged for all experimental conditions. It was fixed to a vertical pipe that was in turn fixed to the main bridge. The ADV was mounted 4.2^o from vertical and 4.8^o from the along tank direction. The ADV data were subsequently corrected for these small deviations in orientation. The ADV was sampled at 25Hz for a duration of 409.6 seconds and recorded fluid velocity in 3 perpendicular directions (along tank, cross tank, and vertical), hydrostatic pressure, and water temperature.

Infra-Red Camera –An infrared camera was mounted on the railing of the main bridge (figure 2). The camera was a FLIR SC6000. It has a 520x640pixel detector that is sensitive in the 8μm to 9.2μm wavelength range of the electromagnetic spectrum (far infrared field). The temperature resolution of the sensor is less than 35mK. The imaging footprint was 73.6cm (along tank) by 92cm (across tank). The camera was mounted near the altimeter

such that the resolution and size of the images could be corrected if necessary using the instantaneous distance to the water surface provided by the altimeter. The camera was also mounted 18° from the vertical to avoid thermal reflection from the bridge in the image. The thermal images have been corrected for the minimal distortion incurred. For each run, 10240 temperature images were recorded at a 25Hz rate corresponding to 409.6 seconds of acquisition time. In addition, a digital video camera was placed above the infrared camera with its imaging area encompassing the footprint of the IR camera. The digital video camera recorded visible wavelength images on DV tape for subsequent cross-check if necessary.

All instruments (except the digital video camera) were synchronized using a common electronic start trigger provided by the National Instrument sampling board. Sampling rates were internally controlled.
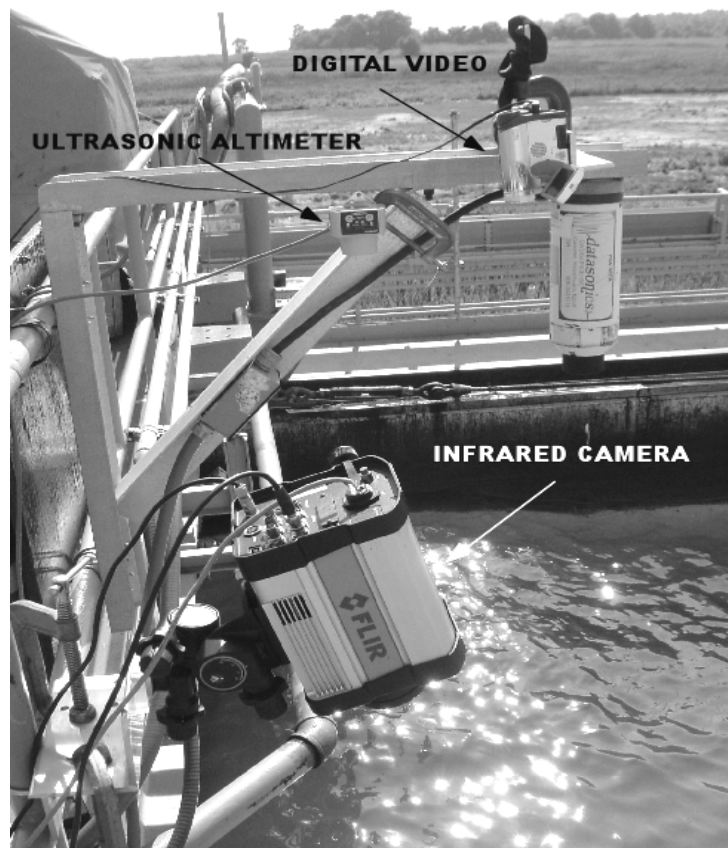
Figure 2: Instrument setup on the main bridge.

Table 1: Experimental conditions studied at Ohmsett. The fetch is taken from the wave paddle and time is local time. The table is sorted with increasing paddle frequency.

Paddle Frequency (Hz)	Experiment #	Date (m/d/y) - Time (h:m:s)	Paddle Stoke (cm)	Fetch (m)
0.33	18	8/19/2008 - 11:05:00	15.3	100
0.33	23	8/19/2008 - 19:10:00	15.3	100
0.47	4	8/18/2008 - 18:00:00	7.65	100
0.47	7	8/18/2008 - 19:12:00	7.65	70
0.4	14	8/19/2008 - 09:10:00	7.65	130
0.50	5	8/18/2008 - 18:30:00	7.65	100
0.50	20	8/19/2008 - 16:20:00	7.65	100
0.50	21	8/19/2008 - 17:58:00	7.65	100
0.50	8	8/18/2008 - 19:30:00	7.65	70
0.50	15	8/19/2008 - 09:25:00	7.65	130
0.50	19	8/19/2008 - 11:20:00	15.3	100
0.55	6	8/18/2008 - 18:45:00	7.65	100
0.55	9	8/18/2008 - 19:45:00	7.65	70
0.55	16	8/19/2008 - 09:54:00	7.65	130
0.55	2	8/18/2008 - 17:00:00	7.65	100
0.58	22	8/19/2008 - 18:10:00	7.65	100
0.58	10	8/18/2008 - 20:00:00	7.65	70
0.58	17	8/19/2008 - 10:10:00	7.65	130
0.67	3	8/18/2008 - 17:20:00	7.65	10
0.67	12	8/19/2008 - 08:32:00	7.65	70
0.67	13	8/19/2008 - 08:45:00	7.65	130

Data Processing & Results

Altimeter – For each experiment, the data from the altimeter was processed with standard Fourier techniques. Spectra were calculated using 10s Hanning window with 50% linear overlap and the resulting spectra were truncated at the effective Nyquist of 5Hz. Figure 3 shows the elevation spectra for a fetch of 100m, a wave maker paddle stroke of 7.65cm, and for frequencies of 0.47Hz, 0.5Hz, 0.55Hz, 0.58Hz, and 0.67Hz. The triangles at the top of the figure show the input frequency. At the lowest two frequencies, wave breaking was not observed visually, the peak in the spectra corresponds to the paddle frequency, and the high frequency tails of the spectra show low energy level and exhibit a clear signature of the harmonics of the primary wave frequency. At higher paddle frequency, wave breaking was observed, with increasing breaking rate and breaking amplitude with increasing paddle frequency. Consequently, the tail end of the elevation spectra show increased energy levels. This is presumably a consequence of an increase in non-linear wave-wave interaction and mostly due to multiple (high) frequencies waves generated by surface breaking events. We note however that the spectra show a -2 roll off to the right of the peak, which is significantly higher than the typical -5 roll off expected for wind generated waves in the open ocean. While we do not expect the spectra of the (initially monochromatic) mechanically generated waves in the Ohmsett tank to follow open ocean wind wave spectrum, this difference warrants precaution in interpreting the results presented here in view of applying the findings to the open ocean. For one thing, the high energy levels at high frequencies in the elevation spectra indicate the presence of large amplitude, small wavelength waves, which therefore have a large slope and are highly non-linear. These will likely generate more frequent breaking than would otherwise be present in the field at similar overall, integrated spectra levels, i.e. at similar elevation variances or significant wave height. In other words, at comparable significant wave heights, we expect more frequency breaking events in the Ohmsett tank. This remains speculative and demands further comprehensive testing of breaking rate and whitecap coverage at the Ohmsett facility. A significant sub-harmonic is also observed for the highest paddle frequency.

The frequency spectra from the altimeter were integrated and used to estimate the significant wave height (table 2). Furthermore, since all the instruments were synchronized, it was possible to examine the time series of the altimeter at the precise time where single breakers were detected in the infrared imagery.
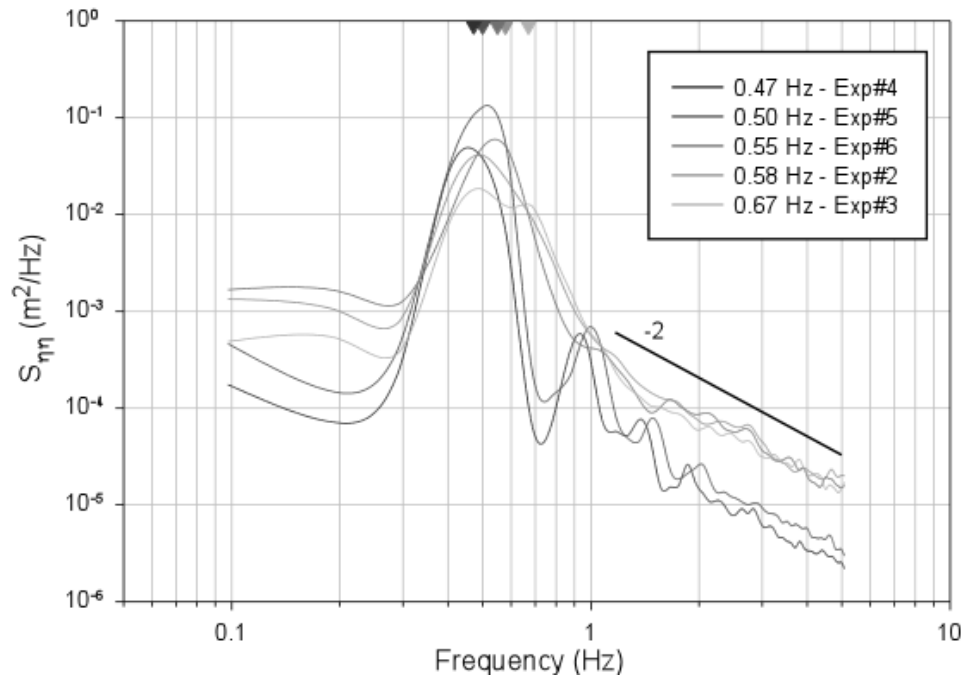
Figure 3: Surface elevation spectra for a fetch of 100m, a wave maker paddle stroke of 7.62cm, and for paddle frequencies of 0.47Hz, 0.5Hz, 0.55Hz, 0.58Hz, and 0.67Hz. The triangles at the top of the figure show the input frequency. The legend also shows the experiment number for reference.

ADV – Similarly to the processing used for the altimeter data, the significant wave height was calculated from the hydrostatic pressure detected by the ADV. Here, because the ADV was placed at a depth 53.3cm, the signal from the high frequency waves (with small wavelength) was significantly damped and did not contribute to the variance in pressure. Consequently, the significant wave height estimated with the ADV is relatively smaller than that detected with the altimeter (Table 2). This is perhaps not surprising, especially in

light of the analysis of the altimeter data showing a significant presence of high frequency surface waves.

In addition, we calculated spectra of the 3 velocity components using a similar technique to that used for the altimeter. The resulting spectra were obtained with a 0.1Hz resolution (10s window) and a 12.5Hz Nyquist frequency. Figure 4 shows the spectra for the vertical component of the velocity for a fetch of 100m, a wave maker paddle stroke of 7.65cm, and for paddle frequencies of 0.47Hz, 0.5Hz, 0.55Hz, 0.58Hz, and 0.67Hz. In each case, the peak spectral frequency matches, as expected, the paddle frequency indicating that most of the energy is injected and remains at the frequency of the paddle. The high frequency tails to the spectra show a -5/3 roll off that is indicative of the presence of an inertial subrange (also sometimes referred to as the Kolmogorov range), the signature of isotropic turbulence. The inertial subrange is the signature of the energy cascade in the turbulence that takes place between the scales at which energy is inputted (wave height/length), and the scales at which energy is dissipated into heat through viscous effect (Kolmogorov length scale). The spectral level in that inertial subrange is only dependant on kinetic energy dissipation and frequency. Under monochromatic waves, the inertial subrange takes the following form:

$$S_{uu}(f) = \frac{7}{110} 2^{4/3} \Gamma\left(\frac{1}{3}\right)\left(\frac{8\varepsilon}{9\alpha}\frac{U_{rms}^{orb}}{2\pi}\right)^{2/3} f^{-5/3},$$

where ε is the kinetic energy dissipation, α the Heisenberg constant (~0.4), U_{rms}^{orb} the root mean squared (rms) orbital velocity, and Γ is the gamma function (Veron and Melville, 1999). We note that this formulation relies on the so called Taylor's frozen turbulence hypothesis which implies that the time scales associate with the turbulence are small compared with the time-scales associate with the mean advecting field (here, the surface waves). This assumption is typically suitable for such measurements but could be violated under weak turbulence and steep short waves conditions.

11

We have used this formula to directly estimate the turbulent kinetic energy dissipation from the spectra (and using the root mean squared orbital velocity also detected by the ADV). The results are presented in table 2. The dissipations measured at 53.3cm depth by the ADV are quite high. We find that the dissipation measured at the ADV depth in the Ohmsett tank under the conditions presented here are significantly higher than observed in the open ocean. For example, if we assume that the dissipation in the ocean follows the "law of the wall" i.e. compares with wall bounded flow, then, when non-dimensionalized, the dissipation scales as:

$$\frac{\varepsilon \kappa z}{u_*^3} = \Delta \ .$$

Here, κ is the Von Karman constant (~0.44), z the depth, u_* the friction velocity (the square of the friction velocity times the density is equal to the surface stress) and Δ=1. Now, it is commonly accepted that the oceanic aqueous boundary layer, mainly because of the presence of surface waves and breaking waves, does not behave entirely similarly to that over a flat rigid surface. In fact, significant departures from the "Law of the wall" are observed and so called enhanced dissipation levels are frequently reported at sea. Nevertheless, assuming that the dissipation measured in the ocean is an order of magnitude higher than that which would be predicted by the "Law of the wall", Δ=10 (a conservative approach, Melville, 1994), we then estimate the equivalent open ocean wind speed which would lead, in the open ocean, to the dissipation rates observed at Ohmsett. The results are presented in table 2 and show that the "equivalent open ocean wind speeds" are nearly all above 10m/s, extending all the way to 30m/s in some cases. Again, this points toward the fact that breaking at Ohmsett, at least in the conditions studied here, is likely more prevalent that would otherwise be observed at sea with similar surface wave conditions. We note that under wind speeds of 10-30m/s, open ocean significant wave heights are upwards of 2m. In the ocean, under the "equivalent open ocean wind speeds" presented here, a significant wave height observed at Ohmsett only occurs at a small fetched of approximately 3-7km. In other words, based on the ADV and Altimeter data alone, we conclude here that the Kinetic energy dissipation and significant wave height conditions at

12

Ohmsett are representative of ocean condition but are consistent with each other only at a fetch on the order of 1 km (O(1)km). In other words, one would expect to find in the ocean, both the dissipation levels and the significant wave height observed at Ohmsett, only at short fetches and under relatively intense winds.
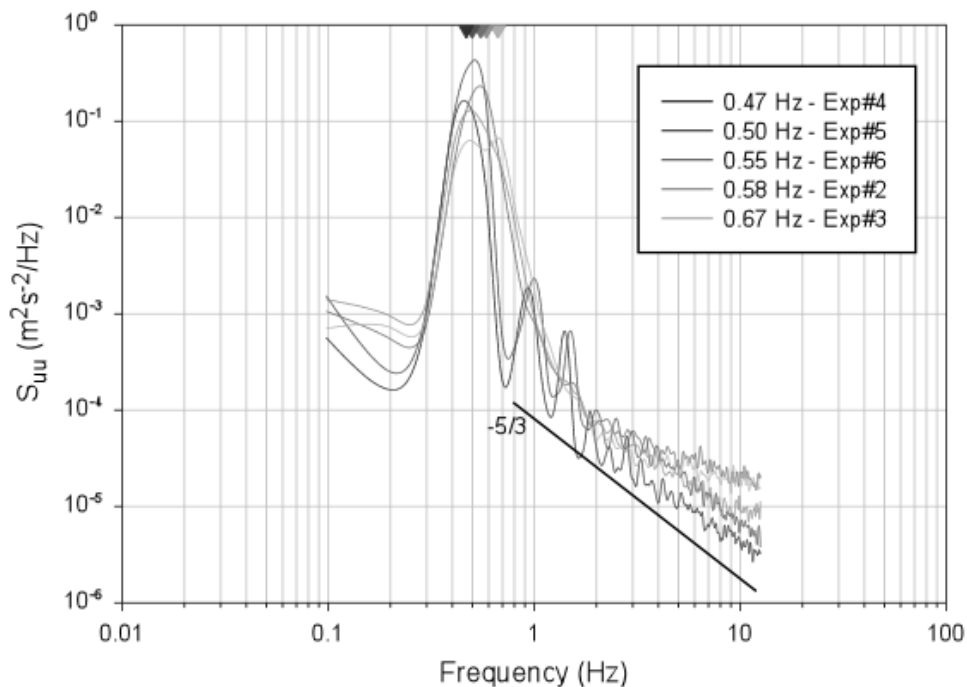
Figure 4: Spectra for the vertical component of the velocity for a fetch of 100m, a wave maker paddle stroke of 7.62cm, and for paddle frequencies of 0.47Hz, 0.5Hz, 0.55Hz, 0.58Hz, and 0.67Hz. The triangles at the top of the figure show the input frequency. The legend also shows the experiment number for reference. The high frequency part of the signal follows the expected -5/3 inertial subrange, signature of the presence of isotropic turbulence.

Another complication arises from the fact that the dissipation measured below the surface is however anticipated to be quite different from that measured directly at the surface. Indeed, as we'll explain in more detail below, the top mm or so of the water is dominated by viscous forces. This leads to the presence of the so-called viscous sublayer

13

that is present near boundaries, even in otherwise turbulent flows. Continuity of (vertical) velocity essentially damps isotropic turbulent eddies and severely inhibits intense turbulence near the surface. Consequently, the turbulence at the surface itself, which is incidentally where the surface contaminant and surfactant reside, will be significantly reduced when compared to levels measured away from the surface. This points towards the need to make direct surface turbulence measurements. This is one of the principal objectives of this work and can only be accomplished, to our knowledge, using fast, high resolution, remote sensing techniques that permit the direct measurements of the water surface motion.

In the next section, we present instrumentation and techniques that allow such measurements of the surface velocity with high spatial and temporal resolution. These techniques are at the forefront of air-sea interaction research and are just beginning to be used in somewhat routine experimental research campaigns in the field and the laboratory. Both the instrumentation and analysis techniques are still being improved upon and are the subject of ongoing research. As such, they both still require a high level of expertise and are not yet suitable for routine deployment in industrial settings.

The use of such infrared techniques and analysis methods provide an elegant, effective, and still unsurpassed way to measure the turbulence at exactly the surface, with high temporal and spatial resolution, and thus even when the surface is deformed (wavy) and moving (see Veron et al., 2008a for details). Direct surface turbulence measurements are extremely difficult and many of the results contain in this report are entirely new.

Table 2: Experimental results for the conditions studied at Ohmsett. Both Significant wave heights (SWH) from the altimeter and ADV are reported. Also shown is the kinetic energy dissipation measured by the ADV and the open ocean equivalent wind speed that would generate such dissipation rates.

Paddle Frequency (Hz)	Experiment #	Date (m/d/y) - Time (h:m:s)	Paddle Stoke (cm)	Fetch (m)	SWH ALT (m)	SWH ADV (m)	Dissipation (m^2s^{-3}) x10^{-4}	Equiv. Wind speed (m/s)
0.33	18	8/19/2008 - 11:05:00	15.3	100	0.45	0.36	2.25	13.11
0.33	23	8/19/2008 - 19:10:00	15.3	100	0.43	0.36	1.68	12.17
0.47	4	8/18/2008 - 18:00:00	7.65	100	0.33	0.21	4.15	15.28
0.47	7	8/18/2008 - 19:12:00	7.65	70	0.27	0.21	0.58	9.23
0.47	14	8/19/2008 - 09:10:00	7.65	130	0.28	0.17	1.78	12.34
0.50	5	8/18/2008 - 18:30:00	7.65	100	0.54	0.27	5.75	16.59
0.50	20	8/19/2008 - 16:20:00	7.65	100	0.56	0.16	1.72	12.25
0.50	21	8/19/2008 - 17:58:00	7.65	100	0.31	0.15	1.48	11.78
0.50	8	8/18/2008 - 19:30:00	7.65	70	0.33	0.38	12.2	20.11
0.50	15	8/19/2008 - 09:25:00	7.65	130	0.31	0.20	1.56	11.94
0.50	19	8/19/2008 - 11:20:00	15.3	100	0.52	0.38	68.4	31.85
0.55	6	8/18/2008 - 18:45:00	7.65	100	0.43	0.25	25.0	24.19
0.55	9	8/18/2008 - 19:45:00	7.65	70	0.44	0.26	5.69	16.54
0.55	16	8/19/2008 - 09:54:00	7.65	130	0.42	0.24	6.11	16.84
0.55	2	8/18/2008 - 17:00:00	7.65	100	0.39	0.22	10.6	19.38
0.58	22	8/19/2008 - 18:10:00	7.65	100	0.43	0.26	5.97	16.75
0.58	10	8/18/2008 - 20:00:00	7.65	70	0.46	0.19	3.14	14.25
0.58	17	8/19/2008 - 10:10:00	7.65	130	0.35	0.26	6.91	17.37
0.67	3	8/18/2008 - 17:20:00	7.65	100	0.30	0.18	27.5	24.82
0.67	12	8/19/2008 - 08:32:00	7.65	70	0.41	0.20	4.06	15.20
0.67	13	8/19/2008 - 08:45:00	7.65	130	0.38	0.20	2.30	13.18

Infrared Camera – Directly beneath the surface is a thin viscous sublayer where the exchange of momentum is principally governed by molecular processes. With the difference between kinematic viscosity and thermal diffusivity being almost an order of magnitude, there is also a thermal sublayer within the viscous sublayer. The thermal sublayer is typically O(0.1-1) mm thick with an O(10)µm top sublayer where heat is exchanged with the atmosphere through radiation. Since the net heat flux from the water (ocean) to the atmosphere is generally positive upward, the surface temperature, or skin temperature, is typically a few tenths of a degree colder than the bulk sea temperature. This leads to what is now referred to as the "cool skin". The Infrared camera provides temperature images of the so-called skin layer at the water surface. At the operating wavelength of the camera (8µm to 9.2µm) the penetration depth of infrared radiation is approximately 20µm. Therefore, the infrared imager detects the average temperature in a surface layer that is 20µm thick. This is well within the thermal and viscous molecular layer at the water surface (at least in all but the most extreme wind and wave conditions).

Turbulence at, or just beneath the surface, will act as local "surface renewal events" disrupting the viscous and thermal molecular layers and bringing parcels of bulk fluid to the surface and in contact with the atmosphere. These parcels of bulk fluid are therefore slightly warmer than the skin layer and appear as warmer patches of water in the thermal images. In a sense, the temperature patterns in the infrared images are a proxy for the time that the parcel of water has been in contact with the atmosphere at the surface: the warmer patches have just been brought up by turbulence, and the cooler patches, have had sufficient time to reach temperature equilibrium. Therefore, assuming that temperature diffusion occurs at time scales much smaller than the advection of temperature anomalies by the velocity and turbulence (an assumption that is obviously rarely violated – never in the work presented here), the surface temperature pattern can then be considered as a passive field and can be used as a proxy field for the surface velocity (and turbulence). Figure 5 shows an example thermal image collected for wave conditions of 0.47Hz with a significant wave height of 0.33m (Exp. 04). No breaking was observed during this experiment and the

surface temperature image is accordingly relatively smooth. Dark gray is cold and light gray is warm; the temperature was not calibrated but our previous experience shows that the temperature range is approximately 100mK under these types of conditions. The small temperature variations are the signs of surface and sub-surface turbulence, or surface renewal events which lead to spatially inhomogeneous residence times of water parcels at the surface and therefore inhomogeneous temperature.
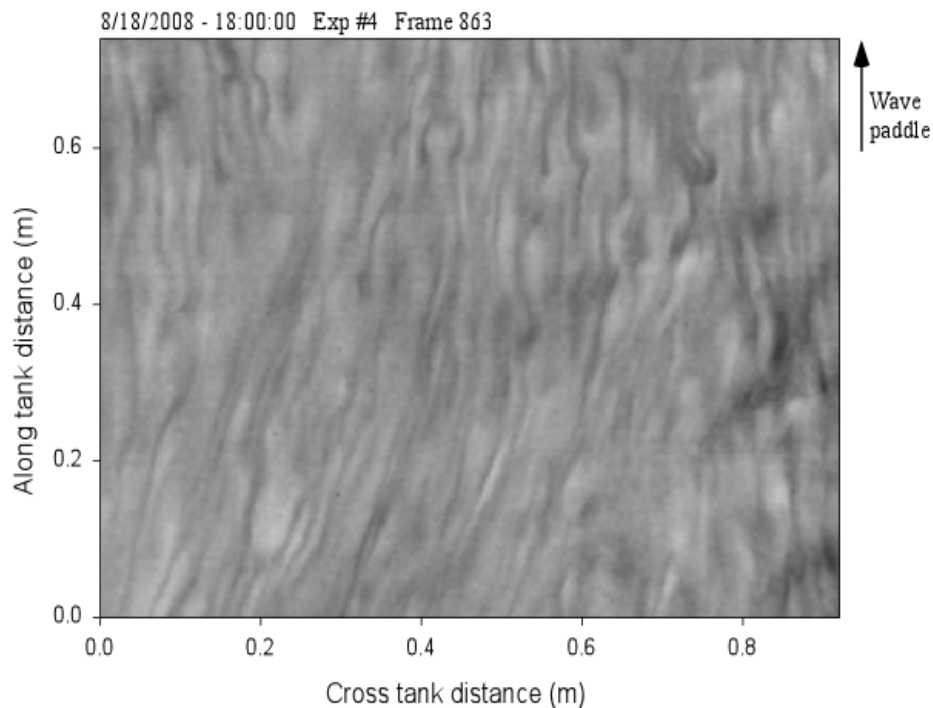
Figure 5: Example of a temperature image taken 8/18/2008 during experiment #4 (small waves and calm conditions – no breaking). Dark gray is cold and light gray is warm; the temperature was not calibrated but our previous experience shows that the temperature range is approximately 100mK. The small temperature variations are the signs of surface turbulence or surface renewal events that brings warm bulk water parcels to the surface where they exchange heat with the atmosphere and cool down.

Infrared Images Analysis - While the temperature variance diminishes with increasing surface turbulence intensity, under the conditions at the Ohmsett tank, and also under typical open ocean conditions, the contrast in the temperature images is sufficient to perform analysis similar to that of particle imaging velocimetry (PIV), on successive surface infrared images. Here we have chosen to use a normalized cross-correlation method that is similar to standard cross-correlation techniques ([Raffael et al., 1998](#)). The normalization compensates for uneven contrast in a single image or sub-image. Also, warmer patterns (light) correlate in the same way as colder patterns (dark) do. In a similar fashion to that of standard PIV routines, we have performed this normalized cross-correlation between sub-images of a pair of temperature images. The cross-correlation allows the identification of a local surface displacement from one image to the other that gives the best possible match. In this case, we used 32x32 pixel sub-images with 50% linear overlap and image pairs separated by 40ms. The cross-correlation sub-image then gives the average displacement between the two sub-images. The average displacement and time difference between the two sub-images then gives the average velocity over the sub-image. In this case, this led to velocity maps at 25Hz containing 1008 velocity vectors (28 x 36). We have tested different techniques to obtain velocity fields including cross-correlation, MQD (Mean Quadratic Difference) and optical flow ([Barron et al., 1994](#); [Gui and Merzkirch, 2000](#)). We found that the differences were small with a slightly better performance of the cross-correlation technique in the sub-pixel regime (using 3 point Gaussian interpolation). The superior computing speed of the cross-correlation technique using FFTs (Fast Fourier Transforms) made this our method of choice. Cross-correlation algorithms have also been used on temperature images in the past ([Garbe et al., 2004](#); [Jessup and Phadnis, 2005](#)). In this implementation, we use a Gaussian interpolation scheme to achieve sub-pixel accuracy on the maximum of the correlation sub-image. Our tests indicate that the rms error in pixel displacement is about 0.05 pixels. Erroneous velocities and outliers are removed from the velocity field using a dynamic mean filter ([Raffael et al., 1998](#); [Thomas et al., 2005](#)). With the resolution of the infrared imager, this leads to errors of approximately 0.2cm/s in the surface velocities. The time interval between images can be

adjusted depending on the surface current and other environmental conditions. We have found here that a 40ms time interval (every infrared image) led, in most cases, to sufficient displacements to avoid significant errors arising from the subpixel interpolation.

In addition to measuring the velocity field with order O(1)cm resolution we can also compute the mean surface current by averaging over the image. We can also infer the surface vorticity, shear strain and divergence fields at centimeter scales, using central difference schemes applied to the velocity fields. With these tools, the surface velocity fields and other higher order surface kinematic fields can be examined in more detail. In particular we will look at the vorticity

$$\omega = \frac{\partial u}{\partial y} - \frac{\partial v}{\partial x},$$

the divergence

$$D = \frac{\partial u}{\partial x} + \frac{\partial v}{\partial y},$$

and the turbulent kinetic energy dissipation

$$\varepsilon = 3\nu \overline{\left(\left(\frac{\partial u}{\partial x} \right)^2 + \left(\frac{\partial u}{\partial y} \right)^2 + \left(\frac{\partial v}{\partial x} \right)^2 + \left(\frac{\partial v}{\partial y} \right)^2 + 2\left(\frac{\partial u}{\partial y} \frac{\partial v}{\partial x} \right) + \frac{2}{3}\left(\frac{\partial u}{\partial x} \frac{\partial v}{\partial y} \right) \right)}.$$

Here, u is the along channel velocity, v, the cross channel velocity, ν the kinematic viscosity of water and the overbar denotes averaging over the image footprint. We note that the dissipation formula above is a simplification of the full formula that involves all terms in the gradient tensor (i.e. the derivative of all the velocities in all directions). At the surface however, only the two-dimensional surface parallel velocities are available (there is no obvious way to measure the small scale vertical velocity and its derivatives); as such, some assumptions on the isotropic nature of the turbulence have been made in order to estimate the missing terms as a function of the measureable variables. These assumptions may not be strictly valid at the surface but provide nevertheless the best way, to date, to estimate the kinetic energy dissipation directly at the surface.

Non breaking surface waves

Figure 6b shows an example of the velocity field calculated using the PIV algorithm on a pair of passive infrared images collected for wave conditions of 0.47Hz with a significant wave height of 0.33m (Experiment 04 – see figure 5). The velocity field is shown with the arrows and is overlaid on the corresponding temperature image (Figure 6a). The velocity field is smooth and continuous and with surface velocities on the order of O(1)cm/s. Higher velocities are obviously observed as non-breaking waves propagate under the field of view but these generally still present smooth and continuous fields, at least in conditions where breaking is not present. A better way to examine the velocity in these cases is to look at the velocity anomaly, i.e. the velocity deviation from the image mean; or to look at local differences such as vorticity of divergence. We show in figure 6c and 6d the vorticity and divergence fields obtained from the velocity the data of figure 6b. Positive vorticity indicates that the vorticity vector points upward out of the water and positive (resp. negative) divergence indicates upwelling (resp. downwelling). The vorticity and divergence fields also are smooth and show the signature of the relatively large scale and slow motion associated with the weak surface turbulence. Here both the vorticity and divergence are on the order of 0.1 to 0.2Hz indicating that the surface renewal events, or the eddy turnaround time in the near surface turbulence is on the order of 5-10s. This is fairly slow but expected and in this particular image, the kinetic energy dissipation is indeed measured at $\varepsilon=1.5\ 10^{-8}$ m^2s^{-3}. We note from visual inspection of the infrared data that these slow, large scale, vorticity and divergence patterns are mostly associated with the passing surface waves of scales smaller or equal to that of the dominant surface waves. These waves provide stretching and compressing of the surface viscous layer and lead to the presence of surface vorticity and divergence. In turn, the turbulence at, and near the surface is stretched and compressed by the passing waves leading to linear and non-linear exchange of energy between the turbulence and the background oscillating velocity field induced by the waves. This energy exchange is a mechanism by which surface turbulence can be generated but it is not significant for small wave slopes (Veron et al., 2009).
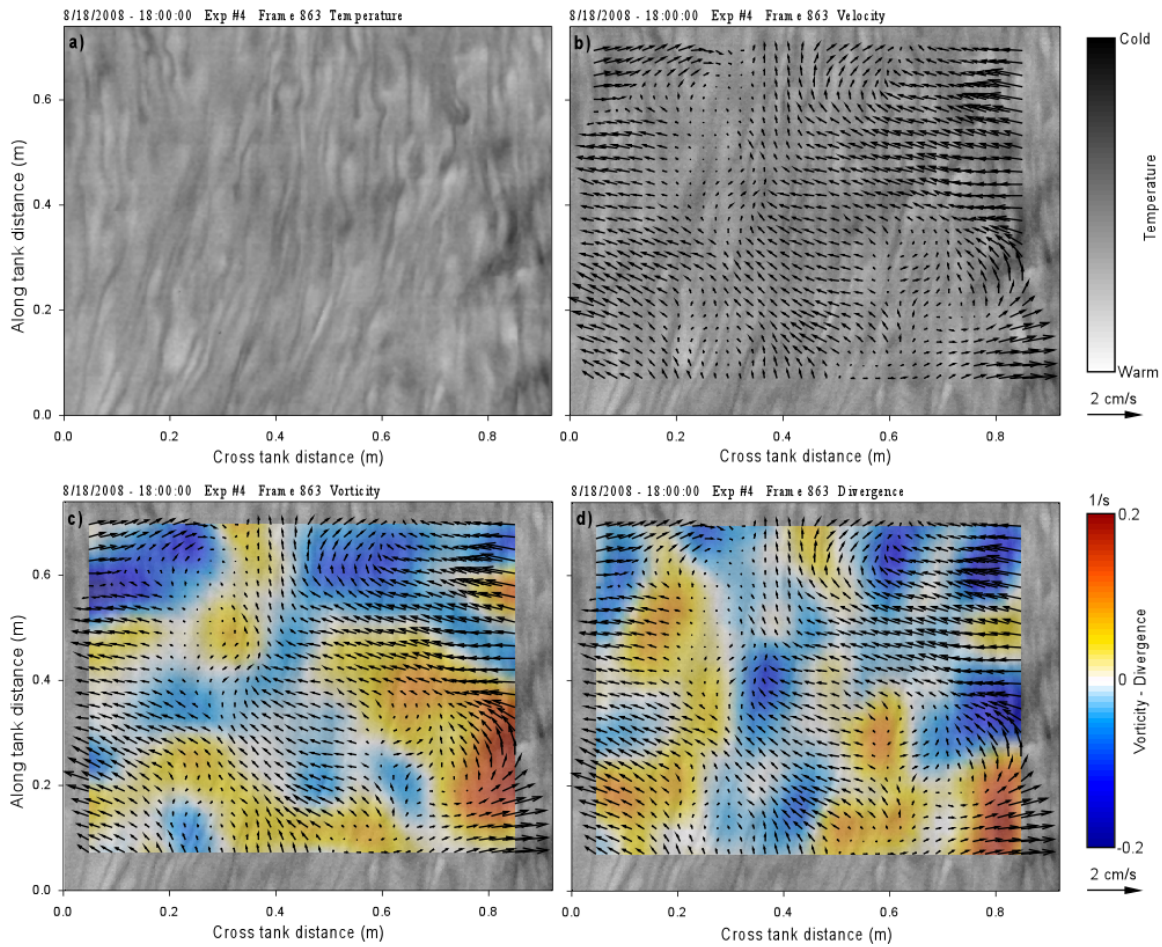
Figure 6: a) Example of a temperature image taken 8/18/2008 during experiment #4 (Figure 5). b) Shows the surface velocity field associated with displacement of passive temperature pattern taken between successive Infrared images (25Hz). c) Shows the vorticity field and d) the divergence field associated with the surface velocity. Positive vorticity and divergence is directed upward.

21

Breaking surface waves

Figure 7 shows a series of infrared images taken while a breaking wave is passing through the field of view. This particular breaking wave is from experiment 06 at t=145.96s after the beginning of the acquisition and is representative of all breaking events observed. During this experiment, the wave paddle frequency was 0.55Hz and the measured significant wave height was 0.43m. Also, some breaking was observed under these conditions and approximately 13 breaking event were visually counted to occur within the foot print of the infrared imager. This will be discussed in more detail below. Figure 7 shows a sequence of infrared images taken every 0.08s (every other infrared image). On the first image, small warm water droplets ejected from the incoming breaking front are already visible. These droplets subsequently impact the surface ahead of the breaking front and generate small capillary rings that are visible in subsequent images. The breaking wave is entering the field of view from the upper right corner of the image and is clearly visible as an intense warm patch of water that is travelling at approximately 80cm/s across the image. The breaking wave front appears warmer as it continuously carries fluid from the bulk fluid to the surface. The temperature contrast in the active turbulent wake of the breaking wave is nearly lost as the intense surface turbulence that is present there does not allow for significant surface residence time and therefore does not allow for significant molecular heat flux from parcels of water that have just been brought up to the surface from the bulk fluid. The thin molecular surface skin is completely destroyed by the passing surface breaking wave front. We note however that only actively breaking waves provide such complete renewal of the surface film. In the field, the fractional area coverage that is influenced by such events can be estimated from the length of breaking fronts (per unit surface area) and from the duration of active breaking (typically a fraction of the wave period) (Mueller and Veron, 2009a). These parameters have not been assessed at Ohmsett.
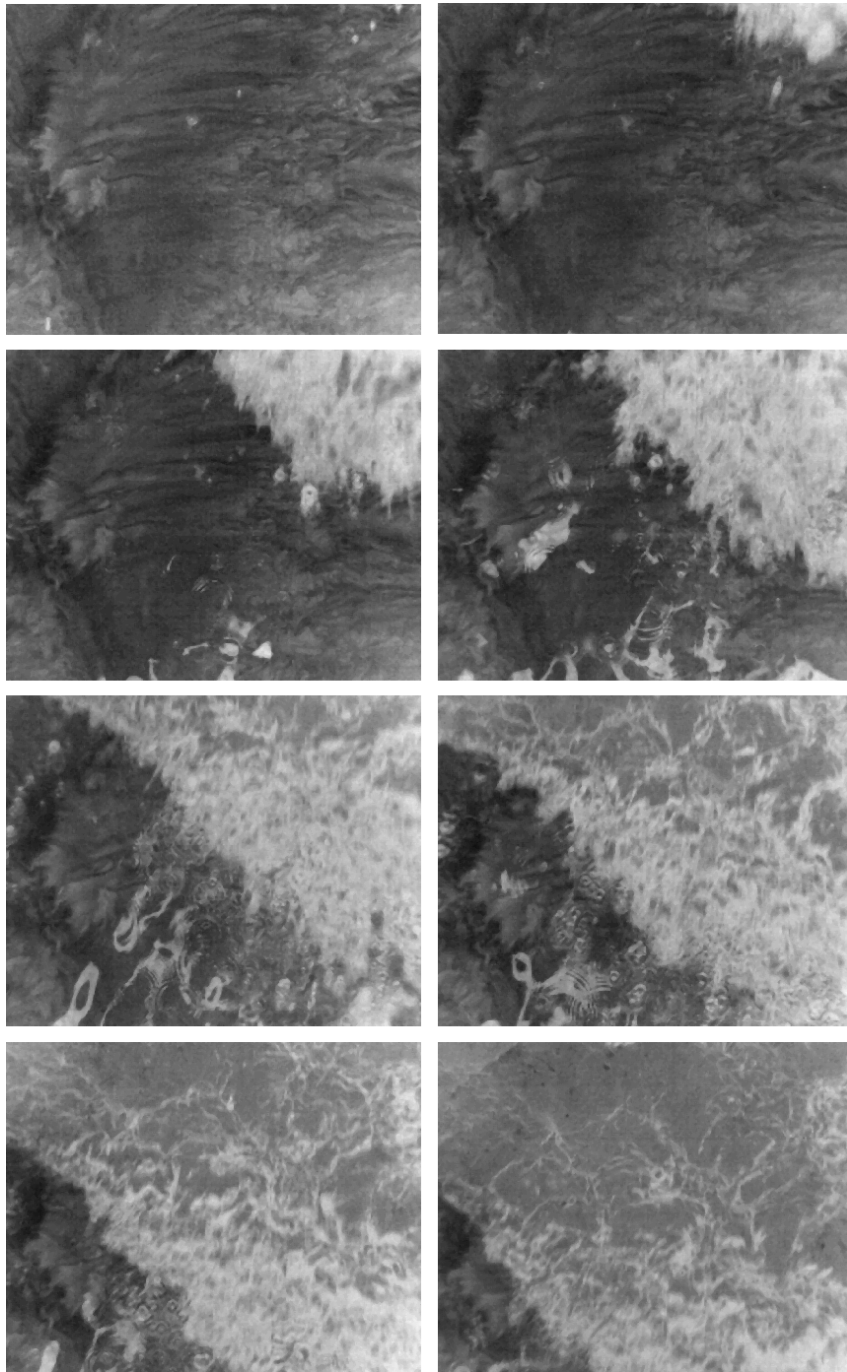
Figure 7: Series of infrared images showing a breaking wave t=145.96s into experiment 06. The sequence shows images every 0.08s (every other infrared image). On the first image, small warm water droplets ejected from the incoming breaking front are visible. These subsequently impact the surface ahead of the breaking front and generate small capillary rings that are visible.

23

Figure 8a shows the velocity field that is estimated from a pair of temperature images taken at t=146.12s into experiment 06 (the 3rd image from the sequence shown in figure 7). At t=146.12s the breaking front has advanced and the breaking wake covers approximately 1/3 of the image. The velocity field is not smooth as it shows a significant jump across the breaking front. This is to be expected in breaking waves where the breaking advancing bore typically propagates forward at a speed that is a fraction of the wave phase speed. Here the velocity of the breaking front is approximately 80cm/s. Also, we show in figure 8b the divergence field overlaid with the velocity. First, we observe an intense negative divergent front congruent with the breaking wave. This simply indicates that water at the surface ahead of the breaking front is being engulfed and submerged as the breaking front propagates. Also, right behind the breaking front is a region of high positive divergence (upwelling) where the turbulence (and conservation of mass) requires that water be brought to the surface to make up for the elevation change associated with the breaking waves. This is similar to what would be observed in a steady hydraulic jump. In addition, we note here that the levels of divergence (and vorticity – not shown) are, in the actively breaking region, on the order of 30Hz indicating that the timescale associated with the turbulence in such breaking events is on the order of 30ms, an increase by two orders of magnitude when compared to the non-breaking case. We note also that divergence and vorticity at the surface of the ocean have been observed to be or order 1Hz to 5Hz under large fetches (O(100) km) and moderate (~5-10m/s) wind speed conditions (Veron et al. 2008b, 2009). For this particular image, the kinematic energy dissipation rate is estimated at $\varepsilon=1.5 \ 10^{-4}$ $m^{2}s^{-3}$ which is 10,000 times more elevated than that of the non-breaking case above. With this image-averaged dissipation estimate, the Kolmogorov time scale is approximately 80ms which compares favorable with the divergence and vorticity estimates. This simply indicates that it is indeed the turbulence generated by the breaking waves that provides for the surface renewal and consequent destruction of the surface molecular layer that is observed in Figure 8. We remind the reader that the dissipation estimate is obtained over the entire image (which contains non-breaking surface area) and that the image average

24

Kolmogorov time scale is therefore expected to be larger (less intense turbulent eddies) than in the actively breaking region.
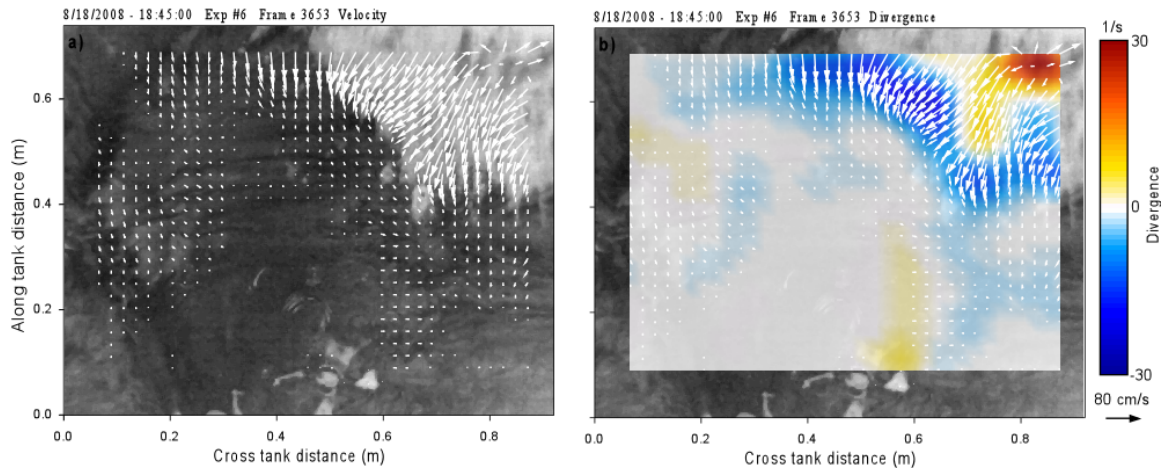
Figure 8: a) Example of the surface velocity during a breaking wave event recorded by the infrared camera at t=146.12s into experiment 06. b) Shows the corresponding divergence field.

We next examine the temporal evolution of the dissipation in the wake, after the passage of the breaking event. This is important because while we can estimate relatively easily the coverage of actively breaking waves at the surface of the ocean under given conditions, in view of estimating which fraction of ocean surface will lead to successful atomization of polluting surface films, we also need to know how fast the turbulence decays in the wake of breaking event. It has been established that the sub-surface turbulent kinetic energy dissipation after breaking, decays roughly as $t^{-5/2}$ at least after the first wave period (Rapp and Melville, 1990). But to our knowledge, no measurements exist (other than those presented here) on the decay of surface turbulence after a breaking event. Figure 9 below shows the temporal evolution of the surface turbulence for the breaking event shown in figures 7 and 8. It shows that there are two distinct phases in the turbulence decay. For the first 4 wave periods, the turbulent kinetic energy dissipation decays relatively slowly as $t^{-2/3}$. This is presumably a sign that the turbulence at the surface is still being sustained by subsurface eddies that continue to act as efficient surface renewal events, even though the

25

turbulence beneath the surface is itself decaying rapidly as energy cascades to smaller scales. After 4 wave periods, the subsurface eddies no longer contain sufficient energy to efficiently combat the laminarizing effects of the viscosity and surface tension and the surface turbulence decays extremely rapidly. In this regime, the turbulent kinetic energy dissipation decays as t^{-4}, much faster than the $t^{-5/2}$ rate observed below the surface where the turbulent eddies are not encumbered and overwhelmed by the presence of the interface. With such rapid decay of the surface turbulence in the wake of a breaking event, we suggest that the relevant parameter, at least when looking at the efficacy of surface breaking waves to atomize and disperse surface pollutant, could be the fractional area coverage of actively breaking waves. We note that the dissipation levels during the -2/3 decay range, which we will name "active wake" is centered about 10^{-4} m^2s^{-3} which is consistent with the results from figure 8 for which the instantaneous dissipation rate was estimated at $\varepsilon=1.5$ $10^{-4} m^2s^{-3}$.
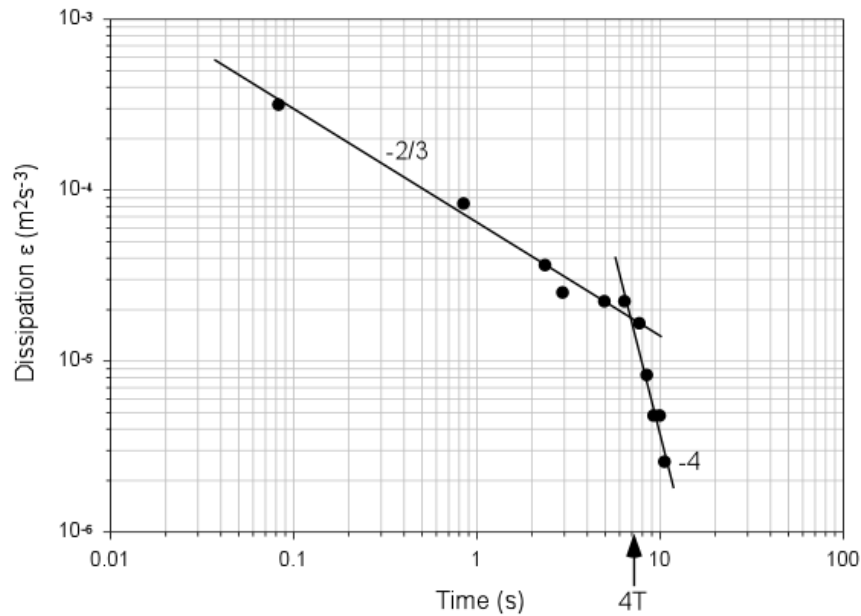

Figure 9 Temporal evolution of the surface turbulent kinetic energy dissipation for the breaking event shown in figures 7 and 8. Two distinct decay phases are visible.

The presence of two distinct regimes in the decay of the turbulence (here the turbulent kinetic energy dissipation rates) in the wake of a breaking event, suggests that the surface can be nearly segregated in two distinct portions: a fractional area covered by actively breaking waves for which the dissipation rates are elevated, and a fractional area where the surface has partially re-laminarized and where surface turbulence is relatively weak and controlled by a balance between surface tension and sub-surface ambient, or shear generated turbulence. Since turbulent kinetic energy dissipation can be calculated on a "per image" basis using the infrared imagery, we construct statistics of the dissipation levels found for each experiment. Figure 10 shows the probability density function (pdf) of the dissipation levels for experiments for experiments 04 and 06, for which no breaking and some breaking were respectively visually observed. Figure 10a shows the pdf of the dissipation collected for the entire duration of experiment 04. The average dissipation for the experiment is 1.4 10^{-5} m^2s^{-3} and the pdf exhibits a log-normal behavior (log normal distributions have previously been observed at depth). Figure 10b shows the pdf of the dissipation in experiment 06 were breaking were observed. The pdf appears to have two distinct peaks that are attributed to the two regimes outlined above. Again, the peak labeled "breaking waves" on the figure is presumably due to the actively breaking waves and their "active wakes". Once more, the level of dissipation there is centered on 10^{-4} m^2s^{-3}. The second peak at the lower dissipation levels is consistent with the dissipation level pdf observed when no breaking is present and is therefore attributed to the background turbulence, or that which remains after the active breaking and wake have passed. The average dissipation for experiment 06 is 4 10^{-5} m^2s^{-3}, which lies between the two peaks from the active breaking and background turbulence.
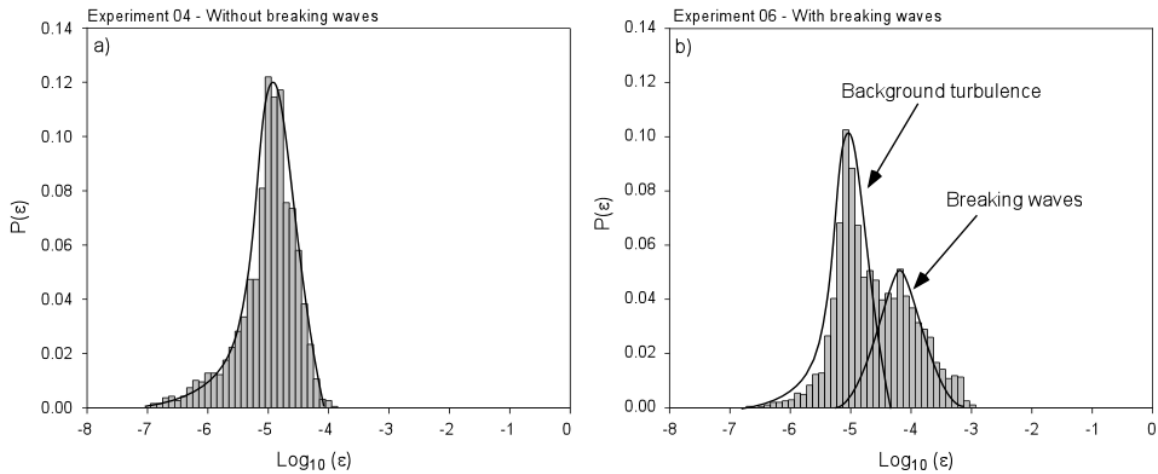
Figure 10 pdf of the dissipation for experiments in which a) no breaking waves were observed and b) breaking was routinely observed. The two regimes in b) are consistent with the two temporal regimes observed in figure 9.

The results presented above are obtained from temporal information and extrapolated to spatial regions of the actively breaking front and wake. Visual examination of the imagery provides a validation of the approach as one can clearly see the smooth calm surface ahead of a breaking front, the breaking front itself and the intense turbulence in the wake as the breaking front propagates out of the imaging footprint. The distance from the breaking front can then only be inferred using the observed breaking front speed (typically a fraction of the wave phase speed) some time before. For field application, we suggest that areal estimate be made directly. With regards to the data collected at Ohmsett and presented here, we can estimate average surface dissipation (for the duration of an experiment), which we tabulated in table 3. However, we would like to suggest caution in reading these results as they are collected temporally, not spatially. This is particularly important in light of the results from the ADV and altimeter which suggest that the wave conditions at Ohmsett are most representative of $O(1)$km fetch conditions.

Table 3: Experimental results studied at Ohmsett. Significant wave heights (SWH) from the altimeter are reported. Also shown is the kinetic energy dissipation estimated from the surface infrared images and related surface turbulent velocity fields.

Paddle Frequency (Hz)	Experiment #	Date (m/d/y) Time (h:m:s)	Paddle Stoke (cm)	Fetch (m)	SWH ALT (m)	Dissipation (m^2s^{-3}) $x10^{-4}$	Comments
0.33	18	8/19/2008 - 11:05:00	15.3	100	0.45	0.07	No visible breaking
0.33	23	8/19/2008 - 19:10:00	15.3	100	0.43	0.13	Harbor Chop - breaking
0.47	4	8/18/2008 - 18:00:00	7.65	100	0.33	0.14	No visible breaking
0.47	7	8/18/2008 - 19:12:00	7.65	70	0.27	0.11	No visible breaking
0.47	14	8/19/2008 - 09:10:00	7.65	130	0.28	0.08	No visible breaking
0.50	5	8/18/2008 - 18:30:00	7.65	100	0.54	0.13	No visible breaking
0.50	20	8/19/2008 - 16:20:00	7.65	100	0.56	0.30	Harbor Chop - No breaking
0.50	21	8/19/2008 - 17:58:00	7.65	100	0.31	0.17	Harbor Chop - No breaking
0.50	8	8/18/2008 - 19:30:00	7.65	70	0.33	0.09	No visible breaking
0.50	15	8/19/2008 - 09:25:00	7.65	130	0.31	0.10	No visible breaking
0.50	19	8/19/2008 - 11:20:00	15.3	100	0.52	0.93	Frequent breaking
0.55	6	8/18/2008 - 18:45:00	7.65	100	0.43	0.40	Little breaking
0.55	9	8/18/2008 - 19:45:00	7.65	70	0.44	0.27	Little breaking
0.55	16	8/19/2008 - 09:54:00	7.65	130	0.42	0.33	Little breaking
0.55	2	8/18/2008 - 17:00:00	7.65	100	0.39	0.31	Some breaking
0.58	22	8/19/2008 - 18:10:00	7.65	100	0.43	0.38	Harbor Chop - Frequent breaking
0.58	10	8/18/2008 - 20:00:00	7.65	70	0.46	0.39	Some breaking
0.58	17	8/19/2008 - 10:10:00	7.65	130	0.35	0.29	Some breaking
0.67	3	8/18/2008 - 17:20:00	7.65	100	0.30	0.26	Frequent breaking
0.67	12	8/19/2008 - 08:32:00	7.65	70	0.41	0.65	Frequent breaking
0.67	13	8/19/2008 - 08:45:00	7.65	130	0.38	0.39	Frequent breaking

Comparison of Ohmsett Measurements to Field Collected Data

The results from the ADV and Altimeter data show high level of subsurface turbulence with low (when compared to open ocean conditions) significant wave heights. This is representative of highly forced, steep waves, found under strong winds and short fetches. One way to represent the state of the sea is to calculate the wave age (W_{age}). The wave age is defined as:

$$W_{age} = \frac{c_p}{u_*}$$

where c_p is the phase speed of the peak wave and u_* is the friction velocity in the air (Bourassa et al. 1999). Young seas or growing waves are associated with small values of the wave age and old seas such as swell are associated with large values of the wave age. Young seas are dominated by wind-driven gravity waves typically have a wave age of less than 28. In the data presented here, the equivalent wave age that would be found in the field and lead to similar conditions as were observed at Ohmsett, range from 4 to 12. In other words, the measured sub-surface turbulent kinetic energy dissipation levels at Ohmsett along with the wave measurements indicate that the facility is well suited for tests representative of young seas.

The kinetic energy dissipation rates and turbulence at the surface are more difficult to relate to the field. This is in part due to the fact that the measurements presented here are unique. There are indeed, to our knowledge, no other direct measurements of surface turbulence in the field, and with this level of detail. In fact, as we mentioned earlier, direct surface turbulence measurements are extremely difficult to make and many of the results contain in this report are entirely new. Some work however (Veron at al. 2008b) allows for partial comparison to field situation and accompanying estimates. For example, instantaneous vorticity estimates in the field, under wind speeds of 3 to 10m/s were observed to be, on average, on the order of O(1-5)Hz. Comparing this with the instantaneous estimates under non breaking waves conditions (Figure 6) and breaking wave

conditions (Figure 8), indicates that, in order to compare to the field, the conditions at Ohmsett would require approximately 16% of the surface to be covered by active breakers. (To match the measured field average of 5 Hz, you need 30HzX+0.2Hz(1-X)=5Hz where X is the fractional surface area that is covered with an active breaker giving 30Hz and 1-X the remaining surface area giving 0.2Hz; X=15.89%). Using the model of Mueller and Veron (2009b), we can also make a theoretical estimate of the surface covered by active breakers at small wave age (~4). Using this model with a short fetch (5 km) and a large wind speed to achieve a wave age of 4 (very young, lots of breakers) the calculated breaker coverage is 11%, for the field. This compares favorably with the Ohmsett results again indicating that the Ohmsett tank compares favorably with field conditions with young seas. However, it is likely that breaking rates at Ohmsett are higher than in the field

Higher statistics can also be used but the field data available are even sparser. We next compare the rms (root mean squared) surface vorticity found at Ohmsett with the data of Veron et al. (2008b). The rms surface vorticity found at Ohmsett are tabulated in table 4 and show mean levels of vorticity on the order of O(1-6)Hz. This compares favorably with the open ocean data of Veron et al. (2008b) shown on figure 11 and would tend to suggest that the results from the Ohmsett experiment compare with open ocean conditions at low to moderate wind speeds (less than approximately 13m/s). This is in slight contrast with the results from the subsurface turbulence measurements that show results typical of strongly forced, young waves. It is difficult to reconcile this two results and this is likely due to the fact that we are now comparing open ocean results (Veron et al. 2008b) to conditions that are best represented by short fetches. While caution should be taken in reading and interpreting these results, it is nonetheless interesting that surface turbulent vorticity levels measured at Ohmsett do compare with those from the open ocean.

Figure 11 Minute long averge of the rms surface vorticity taken from R/P FLIP in the open ocean. Adapted from Veron et al. (2008b).

Table 4: Experimental results studied at Ohmsett. Significant wave heights (SWH) from the altimeter are reported. Also shown is the mean rms surface vorticity over the duration of the experiments. These are to be compared with the results of Veron et al. (2008b).

Paddle Frequency (Hz)	Experiment #	Date (m/d/y) Time (h:m:s)	Paddle Stoke (cm)	Fetch (m)	SWH ALT (m)	Rms vorticity (Hz)
0.33	18	8/19/2008 - 11:05:00	15.3	100	0.45	1.31
0.33	23	8/19/2008 - 19:10:00	15.3	100	0.43	1.66
0.47	4	8/18/2008 - 18:00:00	7.65	100	0.33	2.31
0.47	7	8/18/2008 - 19:12:00	7.65	70	0.27	2.11
0.47	14	8/19/2008 - 09:10:00	7.65	130	0.28	1.57
0.50	5	8/18/2008 - 18:30:00	7.65	100	0.54	2.38
0.50	20	8/19/2008 - 16:20:00	7.65	100	0.56	3.26
0.50	21	8/19/2008 - 17:58:00	7.65	100	0.31	2.63
0.50	8	8/18/2008 - 19:30:00	7.65	70	0.33	1.83
0.50	15	8/19/2008 - 09:25:00	7.65	130	0.31	1.72

0.50	19	8/19/2008 - 11:20:00	15.3	100	0.52	6.09
0.55	6	8/18/2008 - 18:45:00	7.65	100	0.43	3.27
0.55	9	8/18/2008 - 19:45:00	7.65	70	0.44	3.01
0.55	16	8/19/2008 - 09:54:00	7.65	130	0.42	2.99
0.55	2	8/18/2008 - 17:00:00	7.65	100	0.39	2.83
0.58	22	8/19/2008 - 18:10:00	7.65	100	0.43	2.84
0.58	10	8/18/2008 - 20:00:00	7.65	70	0.46	3.17
0.58	17	8/19/2008 - 10:10:00	7.65	130	0.35	3.00
0.67	3	8/18/2008 - 17:20:00	7.65	100	0.30	2.86
0.67	12	8/19/2008 - 08:32:00	7.65	70	0.41	4.18
0.67	13	8/19/2008 - 08:45:00	7.65	130	0.38	3.16

Conclusions

The infrared imagery shows that breaking waves are clearly visible and identifiable as such. The velocity analysis on the images allows for the direct measurements of the breaking front velocity, the surface divergence and vorticity, and the average turbulent kinetic energy dissipation. We observe intense surface renewal (divergence) at the leading edge of a breaking front and we also observe intense turbulence in the (temporal) wake of a breaking event. The turbulence in the wake of a breaker appears to decay in two stages where in a first active stage, the decay rate for the dissipation follows a weak the $t^{-2/3}$ law, and then a much faster t^{-4} law in a second stage. This leads to a conceptual picture of the interface where a fractional surface area is covered with intense turbulence, either from active breakers or active wakes; and a fractional area covered by weaker background turbulence that is presumably set by a balance between subsurface shear generated turbulence and surface tension (Weber number controlled). This picture is corroborated by the pdf of the turbulent kinetic energy dissipation at the surface that shows a bi-modal behavior albeit temporal, not spatial.

The results from the ADV and Altimeter data taken at Ohmsett show high level of subsurface turbulence with low (when compared to open ocean conditions) significant wave heights. This is representative of highly forced, steep waves, found under strong winds and short fetches. The equivalent wave age determined for the conditions studied at Ohmsett, range from 4 to 12. In other words, the measured sub-surface turbulent kinetic energy dissipation levels at Ohmsett along with the wave measurements indicate that the facility is well suited for tests representative of young seas.

The kinetic energy dissipation rates and turbulence at the surface are more difficult to relate to the field. The measured vorticity and dissipations rates at Ohmsett were on the order of 0.1 to 0.2Hz for non-breaking waves and 30Hz for breaking waves. Instantaneous vorticity estimates in the field, under wind speeds of 3 to 10m/s have been observed to be on the order of O(1-5)Hz. Comparing this with the instantaneous estimates under non

breaking and breaking wave conditions at Ohmsett (0.1 to 30Hz, respectively) indicates that, in order to compare to the field, the conditions at Ohmsett would require approximately 16% of the surface to be covered by active breakers. A theoretical estimate of the surface covered by active breakers at small wave age (~4) is 11%. The Ohmsett results compare favorably to the field values for small wave age.

The rms surface vorticity found at Ohmsett compare favorably with the open ocean data of Veron et al. (2008b) and would tend to suggest that the results from the Ohmsett experiment compare with open ocean conditions at low to moderate wind speeds (less than approximately 13m/s). This is in slight contrast with the results from the subsurface turbulence measurements that show results typical of strongly forced, young waves. It is difficult to reconcile this two results and this is likely due to the fact that we are now comparing open ocean results (Veron et al. 2008b) to conditions that are best represented by short fetches. While caution should be taken in reading and interpreting these results, it is nonetheless interesting that surface turbulent vorticity levels measured at Ohmsett do compare with those from the open ocean.

Finally, we note that the results from the Ohmsett tests include direct measurements of the dissipation and associated surface kinematic fields (vorticity and divergence), directly at the surface and over a very short time period: on a "per breaker" basis. Available field data are either taken at depth or evaluate surface kinematics and dynamics over longer times scales. Indeed, the work of Veron et al. (2008b) who initially developed the techniques used here, evaluated surface kinematic fields over times scales of a minute (figure 11) and longer. Direct comparison between instantaneous measurements and longer-term averages are exacerbated by the fact that breaking is a highly intermittent and episodic process. Also, breaking is typically very intense (in terms of turbulence generation and subsequent dissipation) and a few events generally suffice to dominate the long terms averages. Higher order statistics such as variances, skewness and kurtosis from longer term measurement programs may be useful when high temporal data such as those presented here (figure 9) are not available

Recommendations

Based on the analysis of the altimeter data, which showed elevated spectral level at frequencies higher than the peak wave frequency, and therefore a potential for high frequency steep waves and significant non-linear wave-wave interactions, we recommend further and comprehensive testing of breaking rate and whitecap coverage at the Ohmsett facility. This can be relatively easily achieved using visible or infrared imagery technique and the results can be compared with both field data and numerical estimates. The white cap coverage is an important diagnostic and predictive tool since active breakers are the locus of intense surface turbulence generation and both their spatial and temporal distributions allow for direct estimates of statistically relevant parameters such as mean and variances of surface turbulence generation.

It might be useful to further study the turbulence outside the intense breaking regions to evaluate precisely what energy balances control the dissipation levels in the absence of breaking, either in the turbulent active wakes of breakers, or after the active phase. If this were conducted under conditions known to generate effective oil dispersions when chemical dispersants are employed a more precise understanding of the energy levels needed to generate effective (small drop diameter) oil-in-water dispersions could be gained and applied to tests of all scales.

Based on the results of the ADV, and in conjunction with the recommendation above, we suggest that further subsurface turbulence measurements be made at Ohmsett. We find the subsurface turbulence to be high compared to open ocean conditions, albeit consistent with the elevation spectra, but under short fetch conditions. We recommend that the turbulence measurements be made using range sonar (high resolution profilers) rather single point measurements that rely on Taylors frozen field hypothesis. Direct spatial (wavenumber) measurements are preferable for turbulence measurements.

We further recommend that surface measurements of turbulence generated by breakers be conducted in a controlled laboratory setting where wave slope and phase speed can be

36

controlled and repeated. Linear flumes and mechanical breaking waves can achieve a high degree of control and repeatability that would allow for detail measurements. In addition, subsurface turbulence measurement could be conducted simultaneously and surface renewal time scale could be obtained robustly with infrared active techniques (see Veron et al. 2008a). Finally, surface tension could be varied and surfactant introduced.

The open ocean data of Veron et al. (2008b) could be further analyzed to identify single breaking events. High temporal resolution surface measurements of the turbulent kinetic energy dissipation generated by single breaking events could be extracted from this field data as was completed with the Ohmsett data. The field program collected surface elevation (100Hz), meteorological data (25Hz) and surface infrared and video imagery (infrared at 256x256pixels, 60Hz) for 20min per hour and for weeks at a time. The surface conditions encountered (up to 10m/s wind speed) led to significant wave heights of up to 1.8m in a mixed swell, wind-wave sea. Subsurface turbulence measurements were unfortunately not performed. Nevertheless, their data set is the only one that we know of which could yield surface measurements during individual breaking events that could subsequently be compared to the breaking events recorded at Ohmsett.

References

Barron, J.L., Fleet, D.J., & Beauchemin, S. Performance of optical flow techniques. *Int. J. Comp.Vis.* , **12**(1): 43-77. (1994).

Bourassa, M.A., D.G. Vincent, and W.L. Wood,: A Flux Parameterization Including the Effects of Capillary Waves and Sea State. *J. Atmos. Sci.*, **56**, 1123–1139. (1999)

Delvigne, G. A. L. and Sweeney, C. E.: Natural dispersion of oil. *Oil Chem Pollu.* **4**, 281-310. (1988).

Garbe, C.S , Schimpf, U., & Jahne, B. A surface renewal model to analyze infrared image sequences of the ocean surface for the study of air-sea heat and gas exchange. *J. Geophys. Res.*, **109** (C8) doi 10.1029/2003JC001802. (2004).

Gui, L., & MerzkirchmW. A comparative study of the MQD method and several correlation-based PIV evaluation algorithms. *Exp. Fluids*, **28**: 36–44. (2000).

Hinze, J. O.:, Fundamentals of the hydrodynamic mechanism of splitting in dispersion processes. *A.I.Ch.E.J.,* **1**(3): 289–295. (1955).

Jessup, A.T., & Phadnis, K.R.: Measurement of the geometric and kinematic properties of microscale breaking waves from infrared imagery using a PIV algorithm. *Meas. Sci. Technol.*, **16**: 1961-1969. (2005).

Melville, W. K. Energy Dissipation by Breaking Waves. *J. Phys. Oceanog.*, **24** (10): 2041–2049. (1994).

Mueller, J. & F. Veron,: A nonlinear formulation of the bulk surface stress over the ocean through a simple feedback mechanism. *Boundary Layer Meteorology.* **130** (1): 117-134. (2009a).

Mueller, J. & F. Veron,: Dispersive transport model for heavy particles within the marine boundary layer. *Boundary Layer Meteorology.* **130** (2): 229-247. (2009b).

Raffael, M., Willert, C., & J. Kompenhans, J. Particle Image Velocimetry. *A Practical Guide*, Springer, Berlin. (1998).

Rallison, J. M.: The deformation of small viscous drops and bubbles in shear flow. *Annu. Rev. Fluid Mech.*, **16**, 45-66. (1984).

Rapp, R.J, & W.K. Melville, Laboratory measurements of deep water breaking waves. *Phil. Trans. Royal Soc. London*, **331**(1622). (1990).

Stone, H.: Dynamics of drop deformation and breakup in viscous fluids. . *Annu. Rev. Fluid Mech.*, **26**, 65-102. (1994).

Thomas, M., Misra, S., Kambhamettu, C., Kirby, J.T. A robust motion estimation algorithm for PIV. *Meas. Sci Tech.Y*, **16** (3): 865–877. (2005).

Veron, F., & W. K. Melville,: Pulse-to-pulse coherent Doppler measurements of waves and turbulence. *J. Atmos. and Ocean. Technol.,* **16**, 1580-1597. (1999).

Veron, F., W.K. Melville, & L. Lenain.: Infrared techniques for measuring ocean surface processes. *J. Atmos. Oceanogr. Technol.*, **25** (2): 307-326. (2008a).

Veron, F., W.K. Melville, & L. Lenain: Measurements of ocean surface waves and surface turbulence interactions. *J. Phys. Oceanogr., In Press*. (2009).

Veron, F., W.K. Melville, & L. Lenain: Wave-coherent air-sea heat flux. *J. Phys. Oceanogr.*, **38** (4): 788-801. (2008b).